Tunable Supercurrent Through Semiconductor Nanowires

Yong-Joo Doh, *et al.*

Science **309**, 272 (2005);
DOI: 10.1126/science.1113523

Science (print ISSN 0036-8075; online ISSN 1095-9203) is published weekly, except the last week in December, by the American Association for the Advancement of Science, 1200 New York Avenue NW, Washington, DC 20005.

Tunable Supercurrent Through Semiconductor Nanowires

Yong-Joo Doh,[1]* Jorden A. van Dam,[1]* Aarnoud L. Roest,[1,2]
Erik P. A. M. Bakkers,[2] Leo P. Kouwenhoven,[1]
Silvano De Franceschi[1]†

Nanoscale superconductor/semiconductor hybrid devices are assembled from indium arsenide semiconductor nanowires individually contacted by aluminum-based superconductor electrodes. Below 1 kelvin, the high transparency of the contacts gives rise to proximity-induced superconductivity. The nanowires form superconducting weak links operating as mesoscopic Josephson junctions with electrically tunable coupling. The supercurrent can be switched on/off by a gate voltage acting on the electron density in the nanowire. A variation in gate voltage induces universal fluctuations in the normal-state conductance, which are clearly correlated to critical current fluctuations. The alternating-current Josephson effect gives rise to Shapiro steps in the voltage-current characteristic under microwave irradiation.

The recent interest in chemically grown semiconductor nanowires arises from their versatility, which translates into a wide range of potential applications. Many important proofs of concept have already been provided, such as field-effect transistors, elementary logic circuits, resonant tunneling diodes, light-emitting diodes, lasers, and biochemical sensors (*1*–*3*). These achievements, together with the recent advance in the monolithic integration of III-V nanowires with standard Si technology (*4*, *5*), hold great promise for the development of next-generation (opto)electronics. Simultaneously, the high degree of freedom in nanowire growth and device engineering creates new opportunities for the fabrication of controlled one-dimensional systems for low-temperature applications and fundamental science. Quantum confinement and single-electron control have been achieved in a variety of single-nanowire devices (*6*–*8*). In these experiments, the transport properties were dominated by Coulomb interactions among conduction electrons because of the presence of high-resistance barriers either at the interface with the metal leads or within the nanowire itself.

Here we describe an entirely different regime, in which the nanowires are contacted by superconducting electrodes with deliberately low contact resistance. While Coulomb blockade effects are suppressed, the semiconductor nanowires acquire superconducting properties because of the proximity effect, a well-known phenomenon that can be described as the leakage of Cooper pairs of electrons from a superconductor (S) into a normal-type conductor (N) (*9*). The proximity effect takes place only if the S-N interface is highly transparent to electrons. This requirement is particularly hard to meet when the N element is a semiconductor, the major obstacle being posed in most cases by the unavoidable presence of a Schottky barrier. In this respect, indium arsenide (InAs) is an exceptional semiconductor because it can form Schottky barrier–free contacts with metals (*10*). This motivated our choice of this material in the present work.

The InAs nanowires are grown via a catalytic process based on a vapor-liquid-solid mechanism (*11*). The nanowires are monocrystalline, with diameters ranging from 40 to 130 nm and lengths of 3 to 10 μm. From field-effect electrical measurements (discussed below), we find *n*-type conductivity, with an average electron density n_s = (2 to 10) × 10^{18} cm^{-3}, and an electron mobility μ = 200 to 2000 $cm^2/V{\cdot}s$. These values correspond to a mean free path, l = 10 to 100 nm. Right after growth, the nanowires are transferred to a p^+ silicon substrate with a 250-nm-thick SiO_2 overlayer. The conductive substrate is used as a back gate to vary the electron density in the nanowires. Custom metal electrodes are defined by e-beam lithography followed by e-beam evaporation of Ti (10 nm)/Al (120 nm). Before metal deposition, the nanowire surface is deoxidized by a 6-s wet etching in buffered hydrofluoric acid. No thermal annealing is performed, in order to minimize interdiffusion at the contacts. The spacing, L, between the source and drain electrodes is varied between 100 and 450 nm. To perform four-point measurements, both source and drain electrodes are split in two branches (Fig. 1A). A representative single-nanowire device is shown in Fig. 1B.

The nanowire devices exhibit ohmic behavior with a normal state resistance, R_N, in the range from 0.4 to 4.5 kilohms. R_N is virtually insensitive to temperature all the way down to the superconducting transition temperature of the Al-based electrodes, T_C = 1.1 K. Below T_C, the proximity effect manifests itself through the appearance of a dissipationless supercurrent, which can be viewed as a

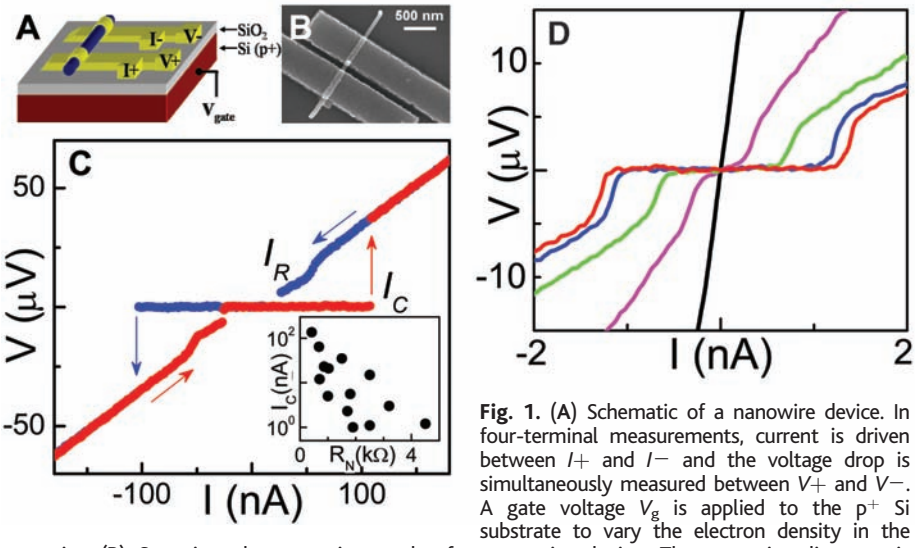

Fig. 1. (**A**) Schematic of a nanowire device. In four-terminal measurements, current is driven between $I+$ and $I-$ and the voltage drop is simultaneously measured between $V+$ and $V-$. A gate voltage V_g is applied to the p^+ Si substrate to vary the electron density in the nanowire. (**B**) Scanning electron micrograph of a nanowire device. The nanowire diameter is determined by the size of the gold catalytic particle, which is visible at the upper end of the nanowire. (**C**) $V(I)$ characteristics for device no. 1 measured in a four-terminal configuration at T = 40 mK for both increasing (red) and decreasing (blue) current bias. (Inset) Correlation between I_C and R_N (the data points correspond to different devices and V_g = 0). (**D**) $V(I)$ characteristics of device no. 2 at T = 40 mK for V_g = 0 (red), –10 (blue), –50 (green), –60 (purple), and –71 V (black). When V_g is made more negative, the critical current is progressively reduced all the way to zero. When the supercurrent vanishes, the zero-bias resistance of the device is 70 kilohms. The characteristic parameters at V_g = 0 are I_C = 1.2 nA and R_N = 4.5 kilohms.

[1]Kavli Institute of Nanoscience, Delft University of Technology, Post Office Box 5046, 2600 GA Delft, Netherlands. [2]Philips Research Laboratories, Professor Holstlaan 4, 5656 AA Eindhoven, Netherlands.

*These authors contributed equally to this work
†Present address: Laboratorio Nazionale TASC-INFM, I-34012 Trieste, Italy.

consequence of the diffusion of Cooper pairs throughout the entire length of the nanowire section between the two superconducting electrodes. (This requires the phase-coherence length for electron propagation in the nanowire to be longer or at least comparable to the distance between source and drain contacts.) To investigate this superconductivity regime, we performed four-terminal dc measurements, in which the voltage across the nanowire, V, is measured while sweeping the bias current, I. In Fig. 1C we show a representative measurement taken at base temperature T = 40 mK. The $V(I)$ characteristic exhibits a clear supercurrent branch (that is, a region of zero resistance) as well as a dissipative quasiparticle branch with a dependence on the sweeping direction of the source-drain current. The switching from superconductive to dissipative conduction occurs when I approaches a critical current, I_C, leading to the abrupt appearance of a finite voltage. The reversed switching, from resistive to superconductive regime, occurs at a lower current level I_R. The observed $V(I)$ characteristics, as well as their hysteretic behavior, are typically found in capacitively shunted Josephson junctions (*12*). (In our devices, the shunting capacitors are formed between the source-drain electrodes and the conductive Si substrate.)

The presence of a supercurrent has been assessed in 14 devices (90% yield) with critical currents ranging from a few nA to 135 nA at 40 mK (see fig. 2S for the temperature dependence). On average, I_C decreases with R_N (inset in Fig. 1C), and the I_CR_N product, a typical figure of merit for Josephson junctions, varies between 2 and 60 μV. The highest value is comparable to the expectation for an ideal S-N-S junction embedding a short and diffusive ($l < L$) normal conductor; that is, $I_CR_N \sim \Delta_0/e$, where Δ_0 = 100 to 120 μeV is the superconducting energy gap of the contact electrodes obtained from finite-voltage measurements discussed below. The semiconductor nature of the nanowires allows the magnitude of the critical current to be controlled by a voltage, V_g, applied to the back-gate electrode (*13–17*). Because of their n-type character, a negative V_g results in a reduction of the electron concentration in the nanowires, leading to a higher R_N and hence a lower I_C. Thus, the nanowires can operate as tunable superconducting weak links. For sufficiently negative gate voltages, I_C is entirely suppressed (Fig. 1D), where the "off" state (I_C = 0) is reached for $V_g \approx -70$ V. This large voltage is due to the weak capacitive coupling between the nanowire conducting channel and the back gate. The use of alternative gating geometries, such as local top gates or gate-around configurations, would provide a much stronger coupling and, at the same time, the possibility of individually controlling different nanowires on the same chip. This would allow a bottom-up assembly of superconducting integrated circuits based on independently addressable S-N-S elements.

To gain more insight into the Josephson behavior of the nanowire S-N-S junction, we investigated the effect of an external microwave field. Because of phase locking between the microwave angular frequency ω_{rf} and the voltage-dependent Josephson frequency (*18*) $\omega_J = 2eV/\hbar$, the $V(I)$ characteristic exhibits voltage plateaus at $V_n = n\hbar\omega_{rf}/2e$, the Shapiro steps (*12*) (here $\hbar$ is Planck's constant, e is the electron charge, and n = 0,±1,±2,…). A representative set of plateaus (up to $|n|$ = 4) is shown in Fig. 2A in the case of 4-GHz radiation. A $V(I)$ curve for the same device in the absence of the microwave field is also shown for direct comparison. We varied the microwave frequencies in the 2- to 10-GHz range in order to verify the proportionality relation between the step height ΔV and ω_{rf}. As shown in the inset in Fig. 2A, the experimental values fall on top of the expected linear dependence $\Delta V = (\hbar/2e)\omega_{rf}$. By increasing the microwave field proportionally to the square root of the externally applied microwave power P_{rf}, higher-order steps become progressively visible and their step width, ΔI_n, exhibits quasi-periodic oscillations. This behavior emerges clearly in a plot of differential resistance, dV/dI, as a function of $P_{rf}^{1/2}$ and source-drain current. In Fig. 2B we show an example of such plots corresponding to the same microwave frequency (4 GHz). The Shapiro steps appear as dark regions (dV/dI = 0) separated by bright (high-dV/dI) lines corresponding to the sharp boundary between consecutive steps. The wiggling behavior of these lines reflects the quasi-periodic oscillations in ΔI_n. These oscillations are quantitatively shown in Fig. 2C for n = 0 to 4. We find good agreement with the theoretical expectation $\Delta I_n = 2I_C|J_n(2ev_{rf}/\hbar\omega_{rf})|$ (*12*), where J_n is the n-th order Bessel function and v_{rf} is the amplitude of rf voltage across the nanowire junction. I_C and a scaling factor, α, for the horizontal axis ($v_{rf} = \alpha P_{rf}^{1/2}$) are the only fitting parameters for all of the five theoretical curves. The observed Shapiro steps represent clear evidence of genuine Josephson coupling through the nanowire.

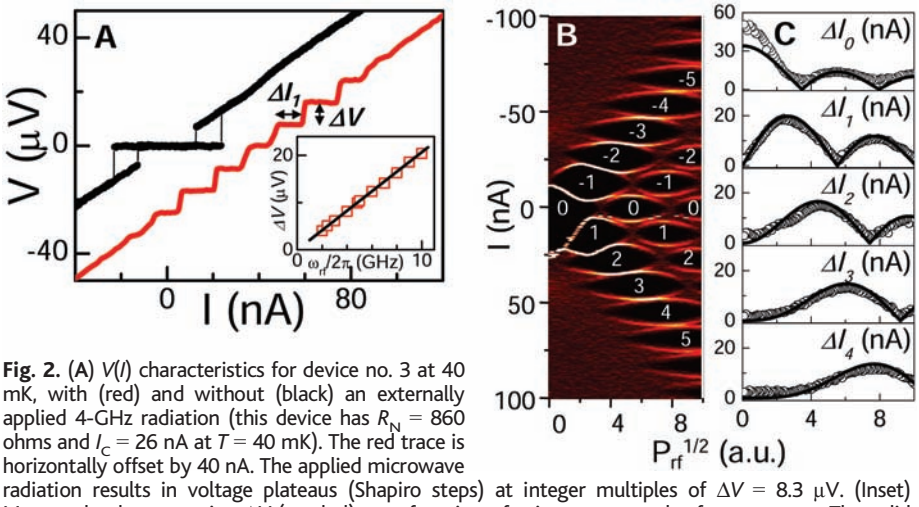

Fig. 2. (**A**) $V(I)$ characteristics for device no. 3 at 40 mK, with (red) and without (black) an externally applied 4-GHz radiation (this device has R_N = 860 ohms and I_C = 26 nA at T = 40 mK). The red trace is horizontally offset by 40 nA. The applied microwave radiation results in voltage plateaus (Shapiro steps) at integer multiples of ΔV = 8.3 μV. (Inset) Measured voltage spacing ΔV (symbol) as a function of microwave angular frequency ω_{rf}. The solid line (theory) shows the agreement with the ac Josephson relation $\Delta V = \hbar\omega_{rf}/2e$. (**B**) dV/dI plotted on a color scale as a function of the bias current I and the square root of the microwave excitation power P_{rf}. In this plot, the microwave frequency is fixed at 4 GHz. The voltage plateaus at $V_n = n\hbar\omega_{rf}/2e$ appear as black regions (dV/dI = 0) labeled by the corresponding integer index n. These regions are delimited by bright lines (high dV/dI) corresponding to the sharp increase of the V between consecutive plateaus. At lower frequencies, we have also observed half-integer steps, such as n = ±1/2, ±3/2,… (fig. S3). (**C**) Current width ΔI_n of the n-th Shapiro steps (n = 0,1,2,3,4) versus $P_{rf}^{1/2}$ as extracted from (**B**). The five solid lines are Bessel-type functions obtained from a single two-parameter fit.

We now discuss in more detail the basic properties of the S-N-S nanowire devices and elucidate their mesoscopic nature. At the onset of the quasi-particle branch (just above I_C), the device conductance is found to be higher than the normal-state value $G_N = 1/R_N$. This is apparent from the slope of the wide-range $I(V)$ characteristic shown in the inset of Fig. 3A (red trace). Only for $V > 0.3$ mV does the slope change to the normal-state value, as becomes clear by a comparison with an $I(V)$ trace taken at 100 mT (black trace), a magnetic field high enough to suppress superconductivity in the electrodes. Evidently, the high-bias linear $I(V)$ at zero field does not extrapolate to the origin, as in the normal state, but to a finite excess current I_{exc} = 0.23 μA. The enhanced conductance at low bias and the consequent excess current provide a clear indication of strong Andreev reflection (*19*): An electron above the Fermi energy coming from the N region is reflected at the S-N interface as a phase-conjugated hole (that is,

the lack of an electron below the Fermi energy) while at the same time creating a Cooper pair in the S region. Andreev reflection at the S-N interface and phase-coherent electron propagation in the normal conductor can be viewed as the microscopic origin of the proximity effect (*10*, *20*). Being a two-particle process, Andreev reflection requires high interface transparency. Under this condition, it enables electrical conduction at subgap voltages, $eV < 2\Delta_0$, where the factor 2 accounts for the presence of two S-N interfaces in series. A subgap conductance, G_{AR}, larger than the normal-state value (up to 2 G_N) can be observed in the case of almost ideal interfaces having a transmission coefficient, T_{int}, close to unity. Shown in Fig. 3A is a plot of the differential conductance dI/dV versus V for the same nanowire device. We find $G_{AR}/G_N \approx 1.4$, and from the value of I_{exc} we estimate $T_{int} \approx 0.75$ (*21*). Similar values are consistently obtained for most of the devices (fig. S4). This high transparency is in line with the best results ever achieved for micrometer-scale superconductor/semiconductor interfaces (*22*). Besides an overall conductance enhancement, the subgap regime is characterized by a series of peaks in dI/dV occurring at $V = 2\Delta_0/me$ (and m = 1, 2, 3) and denoted by vertical arrows. These peaks are due to multiple Andreev processes (*23*–*25*). Between two consecutive Andreev reflections the motion of electron-like (or hole-like) quasiparticles between the two S-N interfaces is diffusive ($l < L$) but phase-coherent.

This mesoscopic character of the nanowire S-N-S junctions emerges clearly from a detailed analysis of the V_g dependence. I_C exhibits reproducible and time-independent fluctuations. In a color plot of dV/dI versus (V_g,I), shown in Fig. 3B, these appear as irregular variations in the I width of the zero-dV/dI supercurrent branch (black region). The superimposed white trace illustrates the evolution of the corresponding normal-state conductance G_N over the same V_g range. Interestingly, $I_C(V_g)$ and $G_N(V_g)$ fluctuations exhibit a clear correlation, which indicates a common physical origin. We interpret these $G_N(V_g)$ oscillations as universal conductance fluctuations (UCFs) (*26*) associated with the phase-coherent diffusive motion along the nanowire. Similar $G_N(V_g)$ fluctuations are also found in the other nanowire devices. The corresponding root mean square (RMS) amplitudes, δG_N, are reported in Fig. 3C. We find an average value of 0.55 e^2/h, which is very close to the expectation for UCF in a phase-coherent quasi–one-dimensional conductor ($\delta G_N = 0.7\ e^2/h$). I_C fluctuations arising from the diffusive motion of electrons in a disordered weak link have been theoretically addressed for two distinct conditions: $\Delta_0 \ll E_{Th}$ (*27*) and $\Delta_0 \gg E_{Th}$ (*28*), where $E_{Th} = \hbar D/L^2$ is the Thouless energy in the normal conductor and D is the diffusion coefficient. In the first case, which is the most pertinent to the present study (Fig. 3C), a universal limit of $\delta I_C \sim e\Delta_0/\hbar$ is expected for the RMS amplitude of the I_C fluctuations, in analogy with universal conductance fluctuations in the normal state. Experimentally, we find δI_C = 0.2 to 3 nA, which is much smaller than the expected value (~25 nA). This discrepancy could be due to non-ideal interface transparency or to an incomplete screening from the electromagnetic environment.

Finally, we would like to comment on the reproducibility of the results presented above as well as on the prospects for nanowire-based S-N structures. About 90% of the devices fabricated in this work have a normal-state resistance below a few kilohms and exhibit a supercurrent branch at low temperature. This indicates reproducibly low contact resistances, an important requirement for successful scaling up to even small superconducting circuits incorporating multiple nanowire devices. The functionalities of these circuits could be integrated with conventional silicon technology or with solid-state quantum computer architectures currently under study. For instance, electrically tunable Josephson nanojunctions may be used as building blocks for superconducting quantum interference devices, in which the circulating supercurrent can be switched on and off by a control voltage. Such devices may serve as switchable coupling elements between superconducting qubits (*29*, *30*). Several important issues still need to be addressed, such as the local gating of individual nanowires and the replacement of Al with wider-gap superconductors allowing for higher operation temperatures. We believe, however, that InAs-based semiconductor nanowires can already provide a convenient basis for the development of more complex hybrid nanostructures, which may enable the investigation of exotic and so-far elusive phenomena resulting from the interplay between size quantization and different types of electron-electron correlations such as superconductivity, Coulomb interactions, and Kondo-type correlations.

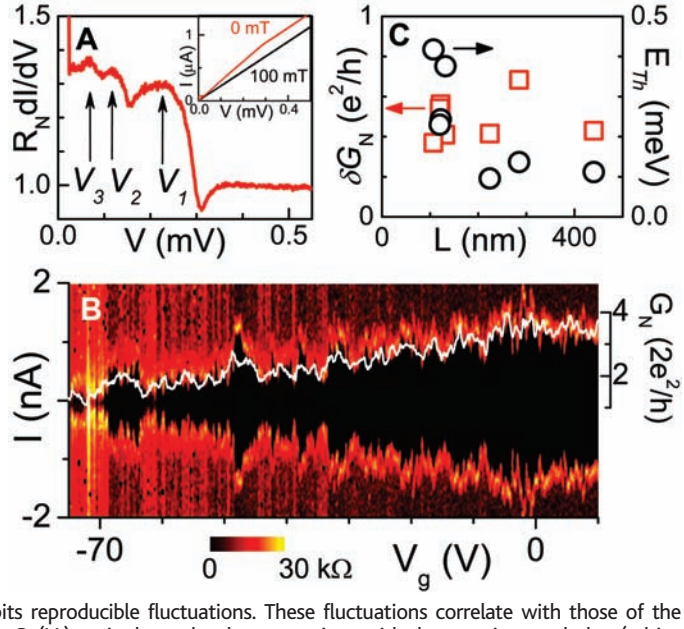

Fig. 3. (**A**) V dependence of dI/dV, normalized to the normal-state value R_N^{-1} for device no. 1. The vertical arrows indicate three dI/dV maxima at $V_m = 2\Delta_0/me$ (m = 1, 2, 3), due to multiple Andreev reflection. (Inset) $I(V)$ characteristics at 40 mK for zero magnetic field (red trace) and for a 100-mT field perpendicular to the substrate (black trace). The supercurrent branch at zero field is not clearly visible in this large bias range. (**B**) dV/dI versus I and V_g for device no. 2. As V_g is varied from 0 to negative values, the supercurrent branch (black region) shrinks and simultaneously exhibits reproducible fluctuations. These fluctuations correlate with those of the normal-state conductance $G_N(V_g)$, as is shown by the comparison with the superimposed plot (white line) sharing the same horizontal scale. [In practice, $G_N(V_g)$ is obtained by measuring dV/dI at $V > 2\Delta_0/e$.] (**C**) The Thouless energy E_{Th} and the RMS value δG_N of the $G_N(V_g)$ fluctuations are plotted as a function of the distance L between source and drain contacts. $E_{Th} = \hbar D/L^2$, where $D = l\ v_F/d$ is the diffusion coefficient for a d-dimensional conductor expressed in terms of the mean free path l and the Fermi velocity v_F. l and v_F are extracted from the mobility, and the carrier density is obtained from the pinch-off $G_N(V_g)$ characteristics (*6*). Because l is typically comparable to the nanowire diameter, we take d = 3 instead of d = 1. Even with this conservative assumption, $E_{Th} \geq \Delta_0$.

References and Notes

1. C. M. Lieber, *Mat. Res. Soc. Bull.* **28**, 486 (2003).
2. P. Yang, *Mat. Res. Soc. Bull.* **30**, 85 (2005).
3. L. Samuelson *et al.*, *Phys. E (Amsterdam)* **25**, 313 (2004).
4. E. P. A. M. Bakkers *et al.*, *Nat. Mater.* **3**, 769 (2004).
5. T. Mårtensson *et al.*, *Nano Lett.* **4**, 1987 (2004).
6. S. De Franceschi *et al.*, *Appl. Phys. Lett.* **83**, 344 (2003).
7. M. T. Björk *et al.*, *Nano Lett.* **4**, 1621 (2004).
8. Z. Zhong, Y. Fang, W. Lu, C. M. Lieber, *Nano Lett.* **5**, 1143 (2005).
9. P. G. de Gennes, *Rev. Mod. Phys.* **36**, 216 (1964).
10. B. J. van Wees, *Phys. World* **9**, 41 (1996).
11. Materials and methods are available as supporting material on *Science* Online.
12. M. Tinkham, *Introduction to Superconductivity* (McGraw-Hill, Singapore, ed. 2, 1996).
13. T. D. Clark, R. J. Prance, A. D. C. Grassie, *J. Appl. Phys.* **51**, 2736 (1980).

14. T. Nishino, M. Miyake, Y. Harada, U. Kawabe, *IEEE Electron Device Lett.* **EDL-6**, 297 (1985).
15. H. Takayanagi, T. Kawakami, *Phys. Rev. Lett.* **54**, 2449 (1985).
16. A. W. Kleinsasser *et al.*, *Appl. Phys. Lett.* **55**, 1909 (1989).
17. C. Nguyen, J. Werking, H. Kroemer, E. L. Hu, *Appl. Phys. Lett.* **57**, 87 (1990).
18. B. D. Josephson, *Phys. Lett.* **1**, 251 (1962).
19. A. F. Andreev, *Zh. Eksp. Theor. Fiz.* **46**, 1823 (1964) [*Sov. Phys. JETP* **19**, 1228 (1964)].
20. B. Pannetier, H. Courtois, *J. Low Temp. Phys.* **118**, 599 (2000).
21. K. Flensberg, J. B. Hansen, M. Octavio, *Phys. Rev. B* **38**, 8707 (1988).
22. A. Chrestin, U. Merkt, *Appl. Phys. Lett.* **70**, 3149 (1997).
23. M. Octavio, M. Tinkham, G. E. Blonder, T. M. Klapwijk, *Phys. Rev. B* **27**, 6739 (1983).
24. E. Scheer *et al.*, *Phys. Rev. Lett.* **86**, 284 (2001).
25. M. R. Buitelaar *et al.*, *Phys. Rev. Lett.* **91**, 057005 (2003).
26. P. A. Lee, A. D. Stone, *Phys. Rev. Lett.* **55**, 1622 (1985).
27. C. W. J. Beenakker, *Phys. Rev. Lett.* **67**, 3836 (1991).
28. B. L. Al'tshuler, B. Z. Spivak, *Zh. Eksp. Theor. Fiz.* **92**, 609 (1987) [*Sov. Phys. JETP* **65**, 343 (1987)].
29. Y. Makhlin, G. Schön, A. Shnirman, *Rev. Mod. Phys.* **73**, 357 (2001).
30. M. J. Storcz, F. K. Wilhelm, *Appl. Phys. Lett.* **83**, 2387 (2003).
31. We thank J. Eroms, R. Schouten, C. Harmans, P. Hadley, Yu. Nazarov, C. Beenakker, T. Klapwijk, B. van Wees, and F. Giazotto. Financial support was obtained from the Dutch Fundamenteel Onderzoek der Materie, the Japanese Solution Oriented Research for Science and Technology program, and the Korean Science and Engineering Foundation.

Supporting Online Material
www.sciencemag.org/cgi/content/full/309/5732/272/DC1
Materials and Methods
Figs. S1 to S4
References

13 April 2005; accepted 25 May 2005
10.1126/science.1113523

Skeleton of *Euplectella* sp.: Structural Hierarchy from the Nanoscale to the Macroscale

Joanna Aizenberg,[1]* James C. Weaver,[2] Monica S. Thanawala,[1] Vikram C. Sundar,[1] Daniel E. Morse,[2] Peter Fratzl[3]

Structural materials in nature exhibit remarkable designs with building blocks, often hierarchically arranged from the nanometer to the macroscopic length scales. We report on the structural properties of biosilica observed in the hexactinellid sponge *Euplectella* sp. Consolidated, nanometer-scaled silica spheres are arranged in well-defined microscopic concentric rings glued together by organic matrix to form laminated spicules. The assembly of these spicules into bundles, effected by the laminated silica-based cement, results in the formation of a macroscopic cylindrical square-lattice cagelike structure reinforced by diagonal ridges. The ensuing design overcomes the brittleness of its constituent material, glass, and shows outstanding mechanical rigidity and stability. The mechanical benefits of each of seven identified hierarchical levels and their comparison with common mechanical engineering strategies are discussed.

Nature fascinates scientists and engineers with numerous examples of exceptionally strong building materials. These materials often show complex hierarchical organization from the nanometer to the macroscopic scale (*1*–*7*). Every structural level contributes to the mechanical stability and toughness of the resulting design. For instance, the subtle interplay between the lattice structure, fibril structure, and cellulose is responsible for the remarkable properties of wood. In particular, it consists of parallel hollow tubes, the wood cells, which are reinforced by nanometer-thick cellulose fibrils wound helically around the cell to adjust the material as needed (*8*). Deformation occurs by shearing of a matrix rich in hemicelluloses and lignin, "gluing" neighboring fibrils, and allowing a stick-slip movement of the fibrils (*9*). Wood is an example that shows the wide range of mechanical performance achievable by constructing with fibers. Bone is another example of a hierarchically assembled fibrous material. Its strength critically depends on the interplay between different structural levels—from the molecular/nanoscale interaction between crystallites of calcium phosphate and an organic framework, through the micrometer-scale assembly of collagen fibrils, to the millimeter-level organization of lamellar bone (*4*, *10*–*12*). Whereas wood is fully organic material, bone is a composite, with about half organic and half mineral components tightly interconnected at the nanoscale. However, nature has also evolved almost pure mineral structures, which—despite the inherent brittleness of most minerals—are tough enough to serve as protection for the organism. In mollusk nacre, for example, the toughening effect is due to well-defined nanolayers of organics at the interfaces between microtablets of calcium carbonate (*5*, *6*). In such structures, the stiff components (usually mineral) absorb the bulk of the externally applied loads. The organic layers, in turn, provide toughness, prevent the spread of the cracks into the interior of the structure, and even confer a remarkable capacity for recovery after deformation (*13*).

Glass is widely used as a building material in the biological world, despite its fragility (*14*–*20*). Organisms have evolved means to effectively reinforce this inherently brittle material. It has been shown that spicules in siliceous sponges exhibit exceptional flexibility and toughness compared with brittle synthetic glass rods of similar length scales (*15*, *20*). The mechanical protection of diatom cells was suggested to arise from the increased strength of their silica frustules (*16*). We have recently described the structural and optical properties of individual spicules of the glass sponge *Euplectella* sp., a deep-sea, sediment-dwelling sponge from the Western Pacific (*21*, *22*). Not only do these spicules have optical properties similar to manufactured optical fibers, but they are also structurally resistant. The individual spicules are, however, just one structural level in a highly sophisticated, nearly purely mineral skeleton of this siliceous sponge (*23*). Here, we discuss the structural hierarchy of the entire skeleton of *Euplectella* sp. from the nanoscale to the macroscale. We show that the assembly of a macroscopic, mechanically resistant cylindrical glass cage is possible in a modular, bottom-up fashion comprising at least seven hierarchical levels, all contributing to mechanical performance. These include silica nanospheres that are arranged into concentric layers separated from one another by alternating organic layers to yield lamellar fibers. The fibers are in turn bundled and organized within a silica matrix to produce flexurally rigid composite beams at the micron scale. The macroscopic arrangement of these beams in a rectangular lattice with ancillary crossbeams is ideal for resisting tensile and shearing stresses. Finally, we identify various structural motifs that provide additional structural benefits to this unique glass skeletal system.

Figure 1A is a photograph of the entire skeleton of *Euplectella* sp., showing the intricate, cylindrical cagelike structure (20 to 25 cm long, 2 to 4 cm in diameter) with lateral ("oscular") openings (1 to 3 mm in diameter). The diameter of the cylinder and the size of the oscular openings gradually increase from the bottom to the top of the structure. The basal segment of *Euplectella* sp. is anchored into the soft sediments of the sea floor and is loosely connected to the rigid cage structure, which is

[1]Bell Laboratories/Lucent Technologies, Murray Hill, NJ 07974, USA. [2]Institute for Collaborative Biotechnologies and Materials Research Laboratory, University of California, Santa Barbara, CA 93106, USA. [3]Max Planck Institute of Colloids and Interfaces, D-14424 Potsdam, Germany.

*To whom correspondence should be addressed. E-mail: jaizenberg@lucent.com